Structural Chemistry
https://doi.org/10.1007/s11224-026-02724-6

RESEARCH

Experimental and computational study of the crystal packing of isoelectronic 4,11-diaza[5]helicene and 4,7,8,11-tetraaza[5]helicene

Giovanni Macetti[1] · **Francesca Fontana**[2,3] · **Monica Panigati**[1,4] · **Simona Rizzo**[5] · **Margherita Vacchini**[1] · **Luca Sironi**[1] · **Leonardo Lo Presti**[1]

Received: 29 October 2025 / Accepted: 7 January 2026

Abstract

The crystal structures of isoelectronic 4,11-diaza[5]helicene (DNH) and 4,7,8,11-tetraaza[5]helicene (TNH) are accurately determined at room temperature by single crystal X-ray diffraction. Analysis of crystal packing with computational chemistry tools, including the evaluation of intermolecular and cohesive energies with force field and charge density (PIXEL) methods, highlights the effect of skeletal replacement of two aromatic C-H with nitrogen atoms. Both crystals are centrosymmetric racemates, with asymmetric units (ASUs) exploiting the same conformation. The ASU of TNH bears two symmetry-independent enantiomers, and the different settings of symmetry operators mirror in different packing motifs with respect to DNH. Both structures exhibit columnar stacking arrangements, which differ in their mutual orientation, distance and strength. Stacking interactions are more frequent and stronger in the tetraaza compound, owing to the greater intrinsic polarization of its ground-state electron density that favors antiparallel arrangements of neighboring molecular dipole moments. Finally, the possible existence of thermodynamically stable chiral forms of the title compounds is investigated by symmetry-constrained Monte Carlo (SC-MC) calculations.

Keywords Azahelicenes · X-ray crystallography · Supramolecular chemistry · Chirality · Crystal structure prediction

Introduction

[n]Helicenes consist of n (>3) ortho-condensed aromatic rings that are forced to adopt a helical configuration due to steric hindrance of the self-folded molecular backbone. The out-of-plane distortion produces a helical motif, which eliminates all the second order symmetry elements characterizing the flat presentation of the molecules. The corresponding enantiomers are designated as P (“plus” or Δ, right-handed) and M (“minus” or Λ, left-handed). The handedness is given by the folding direction of the helicoidal structure, as viewed down the ring closest to an observer that looks along the helix axis (Scheme 1) [1].

Owing to the presence of an intrinsically chiral chromophore and the easy functionalization, [2] [n]helicene derivatives are attractive for a wide range of chemical and materials science applications, including OLEDs [3], metal sensing, [4] photovoltaics, [5] chiroptical switches, [6] asymmetric catalysis [7] and supramolecular chemistry [8]. Even when racemic mixtures are employed, helicene-based materials are employed in semiconductor devices and humidity sensors, [9] along with molecular springs [10] and Covalent Organic Frameworks (COFs) with photoconductive and photo-emitting activity [11]. Incorporation of heteroatoms – particularly nitrogen – in the aromatic backbone allows fine-tuning of electron transport properties and luminescence, [12] even in response to the acid–base environment.

Contribution submitted for the special issue of Structural Chemistry honoring the career of Angelo Gavezzotti.

✉ Giovanni Macetti
giovanni.macetti@unimi.it

[1] Department of Chemistry, Università Degli Studi Di Milano, Via Golgi 19, 20133 Milan, Italy

[2] Department of Engineering and Applied Sciences, Università Di Bergamo, Viale Marconi, 5, 24044 Bergamo, Dalmine, Italy

[3] Consorzio Interuniversitario Per Lo Sviluppo Dei Sistemi a Grande Interfase, Viale G. Marconi, 5, 24044 Bergamo, Dalmine, Italy

[4] Consorzio INSTM, Via G. Giusti 9, 50121 Florence, Italy

[5] CNR-Istituto Di Scienze E Tecnologie Chimiche (SCITEC) “Giulio Natta”, Sede Via C. Golgi, 19, 20133 Milan, Italy

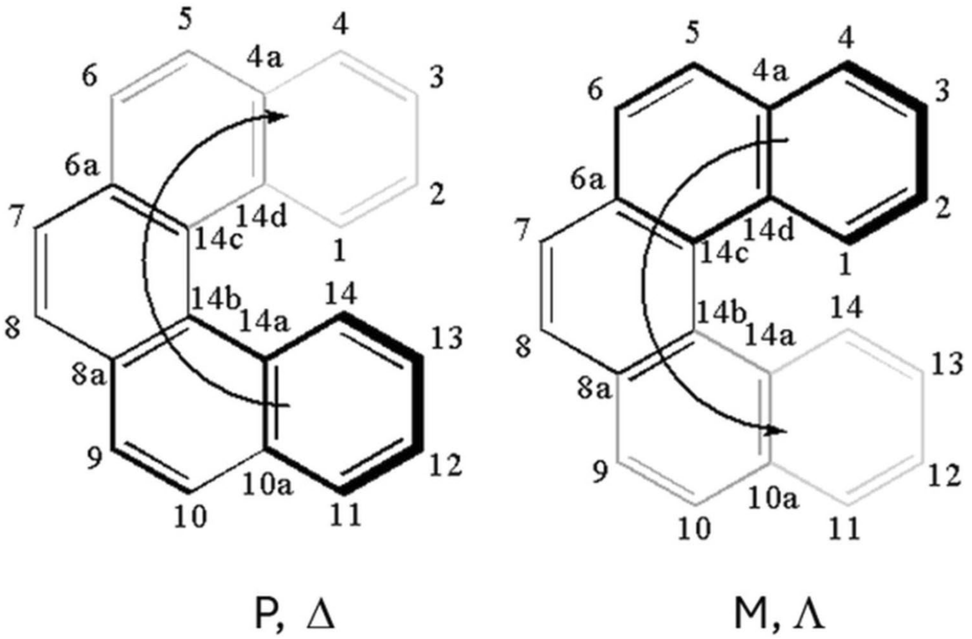

Scheme 1. Chirality descriptors and IUPAc numbering for the [5] helicene scaffold

[13, 14] Recent studies show indeed that azahelicenes are promising circularly polarized luminescence (CPL) emitters and might pave the way toward next gen chiroptical materials. [15, 16]

The solid-state structure of helicene-based systems provides extra degrees of freedom to control their properties. Crystal packing determines not only the optical response (*e.g.* refraction index and birefringence) but also the dynamics of charge carriers and electronic transitions. [17] Moreover, intrinsic spring-like helicity of their molecular backbone is associated with potentially stimuli-responsive mechanical properties. [18, 19] However, experimental investigations specifically focused on the crystallography of these compounds are scanty. To the best of our knowledge, only a few works address the solid-state structures of aza- and diaza-helicenes [20–22], and no X-ray reports even exist on their poly-nitrogenated analogues.

In this contribution, we investigate how and why the substitution of two skeletal C-H in positions 7 and 8 of 4,11-diaza [5]helicene (DNH) with nitrogen impacts on crystal packing. From the viewpoint of the molecular structure, the change is apparently minimal, as 4,7,8,11-tetraaza [5] helicene (TNH) is isoelectronic with DNH and bears exactly the same solid-state conformation (vide infra). However, despite a negligible 0.7% difference in their molecular weights, the TNH crystal is ~ 5% denser than DNH (Table 1), reflecting the setup of packing motifs that are more efficient in the Kitaigorodskii's sense. [23] We here exploit X-ray crystallography and computational crystal chemistry tools to explore and rationalize how supramolecular motifs, and particularly stacking interactions, are affected by the symmetric nitrogenation of the diaza[5]helicene scaffold.

Methods

Synthesis

All solvents were distilled and dried before use. 6-nitroquinoline, glucose, triphenylphosphine are commercial products and were used without further purification. ^{1}H and ^{15}N NMR spectra were recorded on Bruker DRX300 or DRX500 spectrometers. The products were dissolved in $CDCl_3$ or in DMF-d_7. The synthesis of 4,11-diaza[5] helicene was described in [20].

Synthesis of 4,7,8,11-tetraaza[5]helicene (TNH). TNH was prepared following published procedures [24–27]. In particular, 13,2 mmol of 6-nitroquinoline were suspended in 10 mL of 20% aqueous NaOH and heated at 90 °C. To this mixture 12,8 mmol of solid glucose were added portion wise during 30 min. At the end the mixture is diluted with water and extracted three times with 150 mL of CH_2Cl_2, then once with ethyl acetate. Overall, 839 mg of dark green solid, mainly N-oxide derivative with minor amounts of TNH and of N,N-dioxide, are obtained after drying and evaporation of the solvent.

Then, 533 mg of the crude product are dissolved in 20 mL of toluene together with 500 mg of Ph_3P and refluxed for 27 h. After cooling the toluene is removed by evaporation, the solid residue is washed several times with hexane obtaining 490 mg of TNH product. ^{1}H NMR ($CDCl_3$, 298 K, 7.05 T): δ 9.13 (1H, CH(3) dd, J = 4.2 Hz, 1.6 Hz), 9.03 (1H, CH(1) dd, J = 8.5 Hz, 1.6 Hz), 8.87 (1H, CH(6) d, J = 9.0 Hz), 8.48 (1H, CH(5) d, J = 9.0 Hz), 7.45 (1H, CH(2) dd, J = 8.5 Hz, 4.2 Hz) ppm. ^{15}N NMR (DMF-d_7, 298 K, 11.7 T): δ −68 (2N, N(4) and N(11)), + 40 (2N, N(7) and N(8)) ppm.

Table 1 Relevant crystallographic results for DNH and TNH crystals. Full crystallographic information (.cif) files, including PLATON [29] validation reports, are deposited as Supplementary Information to this article

	DNH	TNH
Sample information		
Empirical formula	$C_{20}H_{12}N_2$	$C_{18}H_{10}N_4$
Crystal size, mm^3	0.15 × 0.07 × 0.07	0.36 × 0.09 × 0.09
Formula weight, g·mol^{-1}	280.32	282.30
Crystal system	Orthorhombic	Monoclinic
Space group	*Pbca*, no. 61	$P2_1/c$, no. 14
Z	8	8
Z'	1	2
T, K	293.2(1)	293.2(1)
a, Å	15.8246(2)	14.1140(1)
b, Å	8.76360(10)	17.5038(1)
c, Å	19.9202(3)	11.2428(1)
β°	90.0	107.444(1)
Volume, Å^3	2762.54(6)	2649.78(4)
Density (calculated), g·cm^{-3}	1.348	1.415
F(000)	1168	1168
μ, mm^{-1}	0.623	0.699
Data collection		
λ, Å	1.54184	1.54184
$(\sin\theta/\lambda)_{max}$, Å^{-1}	0.641	0.641
Scan type °	ω-scan, variable speed	ω-scan, variable speed
	0.5	0.5
No. collected reflections	91,605	95,803
No. unique reflections	3003	5772
No. observed reflections, I > 2σ(I)	2876	5229
Refinement results		
Gof	1.121	1.052
Parameters	211	417
R(F), all data/observed data	0.0425/0.0410	0.0477/0.0443
wR(F^2), all data/observed data	0.1072/0.1058	0.1297/0.1261
$\Delta\rho_{MAX/MIN}$, e· Å^{-3}	+0.125/−0.184	+0.271/−0.194

X-ray diffraction

CCDC 2495693 (DNH) and 2495694 (TNH) contain the supplementary crystallographic data for this paper. These data can be obtained free of charge from the Cambridge Crystallographic Data Centre via www.ccdc.cam.ac.uk/structures.

DNH was crystallized from a 1:3 mixture of methanol and acetonitrile, while TNH was crystallized from ethanol; in both cases crystallization was obtained by slow evaporation at room temperature (≈ 24–48 h). X-ray quality crystals were carefully selected by visual inspection on a stereomicroscope. X-ray data collections were carried out at room temperature on a Rigaku Synergy-S four-circle diffractometer mounting a HyPix hybrid photon counter in conjunction with microfocus X-ray sealed tubes. The temperature was chosen to provide an easy comparison with Literature data (vide infra).

Mirror-monochromated Cu Kα radiation (λ = 1.54184 Å) was used throughout, exploiting nominal source power of 50 kV × 1 mA. For both substances, a > 98% complete sphere of reflections was collected up to a resolution of 0.78 Å. Data integration and reduction was carried out with the CrysAlisPro 1.171.43.141a (Rigaku OD, 2024) suite of programs, while the structure was solved with direct methods and refined with nonlinear least-squares procedures implemented in Shelx (Fig. 1) [28]. Table 1 summarizes the relevant crystallographic details of data collections and structural models.

Computational methods

Hirshfeld surface analysis was carried out with CrystalExplorer [30], while Conquest [31] and Mercury [32] were employed to analyze other crystal structures with the [5] helicene scaffold.

The MiCMoS v2.4 suite of programs [33–35] was used throughout to perform both static and Molecular Dynamics (MD) simulations, exploiting experimentally determined X-ray structures as starting points. In all calculations, the C-H covalent distances were normalized to make them comparable with neutron bond lengths [35, 36]. Static lattice energies were computed with either the Lennard–Jones-Coulomb (LJC) force field [37] through the *Crysaa* module of MiCMoS [35] or the PIXEL method, [38, 39] which relies on perturbative MP2/6-31G(p,d) molecular charge densities. Relevant topologies and steering parameters are deposited in the Supporting Information (Section S1 SI). Both CHelpG atomic charges [40] and wavefunction-derived charge densities were obtained by single-point calculations of Gaussian16 [41] on the H-corrected experimental structures. Finally, VMD 1.9 [42] was used to plot MP2/6-31G(p,d)-level molecular electrostatic potential onto the corresponding charge isosurfaces at 0.001 atomic units.

500 ps-long NpT MD simulations [34, 37] were carried out on both DNH and TNH crystal structures at 298 K and 1 atm, using a standard leap-frog integrator with time step of 1 fs. Approximately cubic periodic simulation boxes with edges of ≈ 55–60 Å were employed and a general cutoff of 16 Å was applied for long-range interactions. Thermodynamic boundaries were controlled by a CSVR thermostat with time constant τ = 0.6 ps, [43] and by an anisotropic Parrinello-Rahman barostat with scaling constant ww = 4.0 kg. [44] Results from MD were obtained by averaging the structures over the last 200 ps of the trajectory, when the system is fully equilibrated (see Figure S1 SI). The MD estimates for lattice parameters and density are in good quantitative

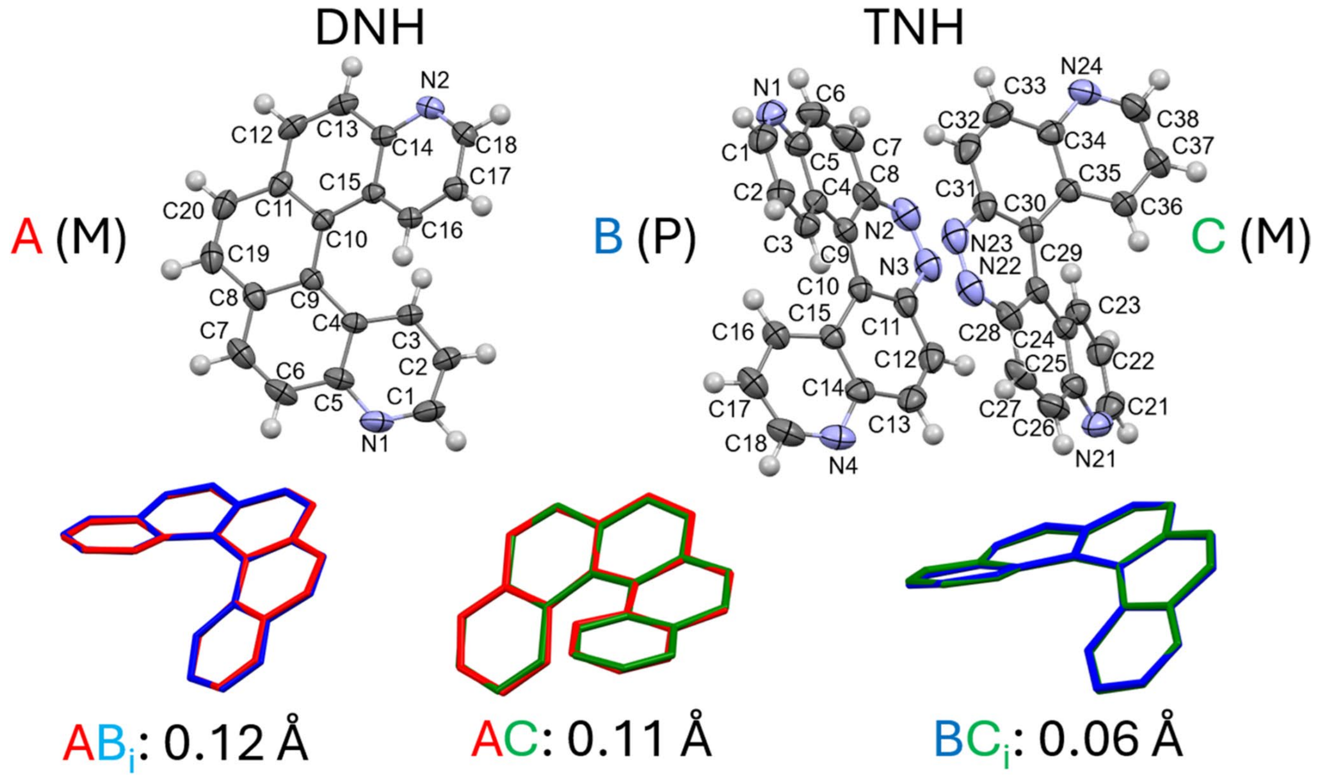

Fig. 1 Up: experimental structure of the asymmetric unit (ASU) of DNH (Z’ = 1) and TNH (Z’ = 2) crystals, with the convenience numbering employed the X-ray structure determination (see also Tables S6-S7 SI). Thermal ellipsoids at RT are drawn at the 40% probability level. Molecules are labeled as A, B and C and highlighted in red, blue and green. The handedness descriptor P or M is also given (see Scheme 1). Down: coordinate RMSD (Å) of different molecular pairings, shown as capped stick representations without hydrogens. An “i” subscript indicates whether that molecule was inverted before calculating the RMSD

agreement with the experiment (Table S4 SI), with relative deviations no greater than + 3.6/−3.4%. This is in line with the expected performance of MiCMoS. [34, 45]

Crystal structure prediction

The recently developed symmetry-constrained Monte Carlo (SC-MC) method [46] was exploited to generate plausible enantiomerically pure crystal structures of DNH and TNH. The purpose is to predict in what aspects the probable crystal packing of pure P/M enantiomers might differ from the racemates of the title compounds. SC-MC generates guess structures by random choices of lattice parameters and mutual molecular orientations. Any guess structure is tested by some hundreds or thousands of steps of symmetry-constrained Monte Carlo, which means that any change affecting any molecular degree of freedom (conformation, rigid-body translations and rotations) is applied to the whole lattice according to user-selected symmetry operators and Bravais translations. If explorative SC-MC produces a potentially stable structure (*i.e.* with negative cohesive energy), the trajectory is further evolved, until convergence is achieved. Predicted crystal structures are ranked according to their cohesive energy; duplicates are found and discarded [47].

As for the title compounds, *NpT* calculations at 298 K and 1 atm with the same LJC force field [37] were carried out, with a 15 Å cutoff for long-range interactions. No internal degrees of freedom were activated, as we assumed that the [5]helicene scaffold is a rigid body. Predictions were restricted to the most common Sohncke groups $P2_1$ (n. 4) and $P2_12_12_1$ (n. 19), up to a maximum of 200 successful structures. Each of these implied 10^3 explorative SC-MC steps, followed by further 10^4 steps for equilibration. Relevant input files are deposited in the Supporting Information (Section S4 SI).

The ten most promising structures in each space group underwent 200 ps-long Molecular Dynamics simulations within the same boundary conditions used for the DNH and TNH experimental structures (298 K and 1 atm, cutoff 16 Å, CSVR thermostat and PR barostat) to check their mechanical stability in terms of RMSD of center of mass and relative molecular rotations with respect to the starting predicted (perfect) structure [46].

Reproducibility

Quantum calculations were carried out with the commercial public Gaussian16 software (https://gaussian.com/). Classical force field simulations were performed with MiCMoS v2.4, while crystal structure predictions were carried out with the related SC-MC 1.0 program. These can be both downloaded free of charge under the specified citation and use conditions, upon registration, from https://sites.unimi.it/xtal_chem_group/. Relevant steering parameters and procedures for both programs are deposited in the Supporting Information (Sections S1 and S4 SI). Main output files, including MiCMoS trajectories and SC-MC predictions, can be downloaded freely from the public repository Zenodo (https://doi.org/10.5281/zenodo.17407385). This ensures full reproducibility of all the calculations here described.

Results and discussion

Molecular conformation

The crystal structure of DNH was determined some 20 years ago as part of a systematic investigation of several diaza[5] helicenes (CCDC BOLMEV, structure **1** in ref. [21]). The present results are in fair quantitative agreement with former ones (Table 1 and Table S1 SI), but the current least squares model is significantly more accurate and precise, as can be appreciated by better intensity statistics and lower crystallographic agreement factor (this work: 0.0410; BOLMEV: 0.0806). To the best of our knowledge, the crystal structure of TNH has never been reported before, but the TNH molecule was present in a co-crystal with perhalooctane (CCDC ECASAE). [48] The most striking difference between DNH and TNH resides in their ASUs, which consist of one formula unit in DNH (Z'=1) and two formula units in TNH (Z'=2).

A survey of the current release of Cambridge Structural Database (v5.46, last update: February 2025) [49] looking for the [5]helicene structure with possible heteroatom and/or substituents in positions 4,7,8 and 11 (Scheme 1) gives only 29 matches (0.002%) under the constraints "only organics" and "single crystal structures". The full list of CCDC refcodes is deposited in the Supporting Information (Table S5 SI). The dihedral angle between the least squares planes passing through the terminal rings can be taken as a measure of the steepness of the helix. Such dihedrals are symmetrically distributed around an average value of ~ 50º with first 25% quantiles ranging from 48º and 52º, and extreme values at 38º (UFENOM) and 60º (XINLIS). The distance between extremal atoms in positions 1 and 14 (Scheme 1) should measure the extension of the molecular spring, also including information on how much the parallel "arms" of the loop are open, and correlates well with the above dihedrals (Figure S2 SI). 1–14 distances also exploit a symmetric distribution, ranging from 2.823 (AVUKUA) to 3.058 Å (XINLIS), with average 2.950 Å.

Figure 1 shows the ASUs of DNH and TNH. The helices are slightly compressed, with dihedral descriptors of 48.11º (DNH) and 45.66º (N1-C18, molecule B) or 47.90º (N21-C38, molecule C) (TNH), that is, below the CCDC average but in line with the expected distribution. Interestingly, 1–14 distances are slightly longer in TNH (DNH: 2.929 Å; TNH: 2.961 and 2.967 Å), as nitrogenation at 7,8 shortens the C-N (8a-8), N–N (8–7)and N–C (7-6a) covalent distances in the central ring by some 0.05 Å (Tables S6-S7 SI). This distortion slightly pushes away the two terminal phenyl groups and increases the 1–14 distances by some 0.03 Å. To the sake of comparison, when TNH is crystallized with perhalogenated n-octane in ECASAE [48], the dihedral is significantly smaller (42.68º) and the 1–14 distance is more like DNH (2.937 Å). This proves that the spatial extension of these compounds can be slightly adjusted, following the requirements of the crystal field, but the structure remains essentially the same, as expected owing to the rigidity of the helix.

Net of these minor differences, all molecules in DNH and TNH bear the same conformation. In fact, DNH and its centrosymmetric image match both molecules in the ASU of TNH, with RMSD of 0.11 Å or 0.12 Å (Fig. 1, bottom). Within the same TNH structure, the two symmetry-independent units are also quantitatively superimposable (RMSD = 0.06 Å) upon application of the inversion operator (Fig. 1, bottom). Otherwise, they score an RMSD of 1.06 Å due to the opposite P/M handedness. At variance with other acentric racemates, the breaking of the inversion center in the ASU of TNH is due to small rigid displacements of the two independent moieties with respect to each other, not to coexistence of different conformers [50].

Crystal packing

DNH and TNH crystallize in centrosymmetric space groups (Table 1) meaning that they are centrosymmetric racemates. They both host a total of 8 molecules in cell, equally divided into right-handed and left-handed enantiomers (Scheme 1). The main reason is that the synthesis procedure was not enantioselective (see Methods). Moreover, it is known from DFT simulations that racemization of [n]helicenes is as much easier as smaller is the number [n] of condensed aromatic rings [51]. As for [5]helicenes, the kinetic barrier was estimated to be 24.4 kcal·mol^{-1}, [51] which is low enough to allow racemization at temperatures close to RT. We did not perform analogue quantum simulations for nitrogenated [5] helicenes, but we have no reasons to believe that the kinetic barrier is greatly different for the title compounds.

Figure 2a-d compares the main features of crystal packing of DNH and TNH through the corresponding Hirshfeld surface fingerprint plots (HSFP). For each molecule, HSFP displays the frequency of internal and external distances (d_i, d_e) in Å of any pair of atoms from the corresponding Hirshfeld surface. [52] Accordingly, color and shape of HSFP depend only on how a certain molecular shape fits into a given packing, allowing one to highlight qualitatively the main features of molecular recognition in that structure. As molecular conformation is identical in DNH and TNH (see above), HSFP here compares directly packing differences on the same grounds.

Parallel sharp spikes at $min[d_i + d_e] \approx 2.4–2.5$ Å are common to both compounds and are due to weak CH···N hydrogen bonded contacts. In molecule A, two lateral "wings" at greater $d_i + d_e$ (≈ 3 Å) are visible, which can be explained by proximity of CH groups with aromatic rings interactions; these are present also in molecules B and C of TNH, although being less appreciable. The most evident difference is due to the bright region along the main diagonal of the TNH fingerprint around 3.8–4.0 Å, which is barely visible – but still present – in DNH. This is the signature of possible π···π stacking interactions, which come with more frequent H···H contacts in TNH. H···H interactions populate the long spike at the centre of the diagram and, being ubiquitarian in molecular crystals, do not bear any specific structural meaning, apart implying that, on average, molecules are packed closer in this structure.

Inspection of real-space crystal packing (Fig. 2e-f) complements and explains the findings from HSFP. Stacking interactions are explored with the aromatic analyser of Mercury (Table S8 SI) [32]. In brief, this is a geometrical analysis that ranks such interactions as "strong", "moderate" or "weak" by comparing the mutual distances and orientations of aromatic rings in each experimental structure with those of benzene pairs whose interaction energies are known at the DFT level in the gas phase. The analysis is qualitative, but results are consistent with both the outcomes from HSFP and Molecular Dynamics (vide infra).

In DNH, some stacking interactions are set up between close-packed molecules with closest rings at ~ 5 Å apart from each other (Fig. 2e). These form columns running along the *a* cell axis, with only one potentially "strong" interaction according to Mercury (red dotted line in Fig. 2e). [32] Along *c*, parallel columns of stacked molecules are connected each other by weak CH···N hydrogen bonds that involve only the

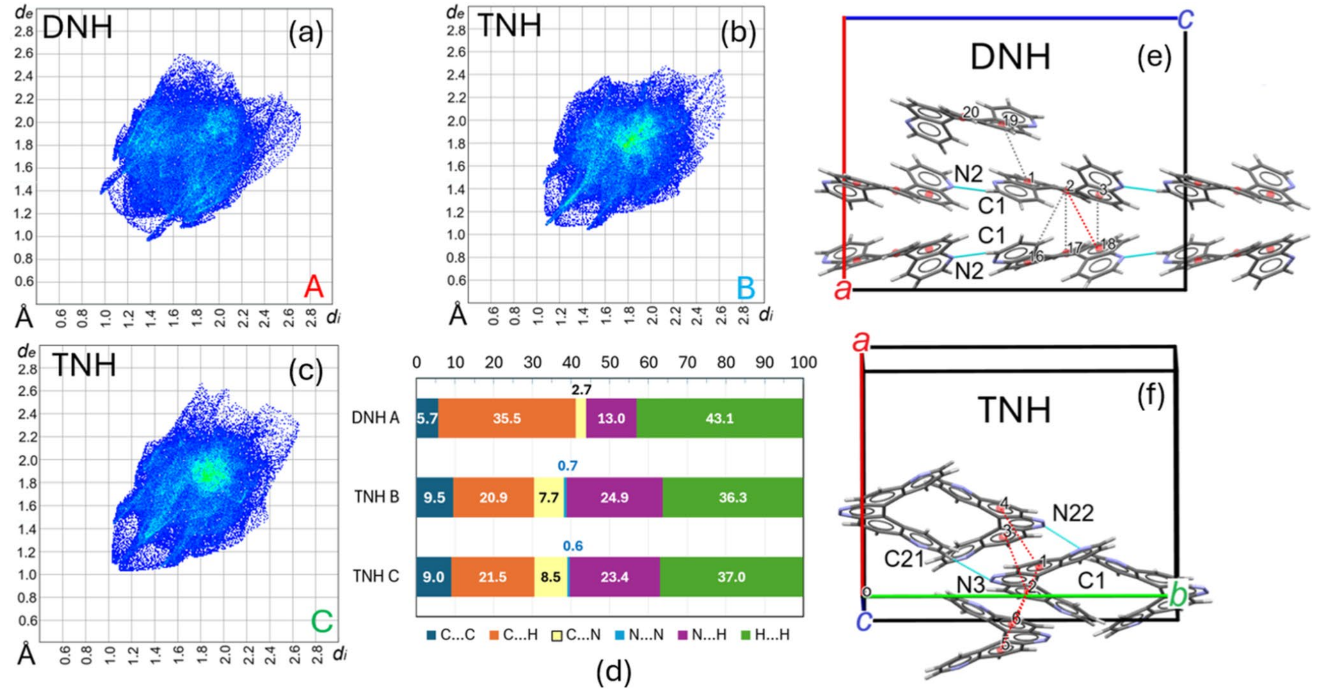

Fig. 2 (a-c) Hirshfeld surface fingerprint plot (HSFP) for symmetry-independent molecules A (DNH) and B, C (TNH) (see Fig. 1). (d) Percent coverage of the HSFP from the various types of atom–atom contacts. (e–f) Relevant intermolecular interactions in the title compounds. Aromatic centroids of coordinated are shown in red, with arbitrary numbering (see Table 2). CH···N hydrogen bonds (Table S9 SI) are coloured in cyan, with labels of donor and acceptor atoms highlighted according to Fig. 1. Dashed lines refer to possible stacking interactions, with colour referring to their expected strength according to the aromatic analyser utility of Mercury (red: "strong"; grey: "moderate") [32]. Aromatics numbering is arbitrary and refers to data in Table S8 SI. (e) DNH, as seen along the monoclinic axis. (f) TNH, as seen roughly along the *c* axis. Only "strong" stacking contacts are shown, as the "moderate" ones cross-link rings also exhibiting "strong" interactions

N2 quinoline nitrogen in position 4 (Fig. 2e, Table S9 SI). Crystallographic glide planes relate such parallel stacked columns along the orthogonal *b* direction (not shown in Fig. 2e).

In TNH, neighbouring molecules lie closer, with nearest rings at ~ 4 Å apart, and form columnar stackings running along the *a* cell axis (Fig. 2f), where alternating enantiomeric pairs are related by inversion symmetry and produce a "zig-zag" pattern. Stacking interactions are possibly more favourable in TNH than in DNH (red dotted lines in Fig. 2e-f). Along the monoclinic axis *b* of TNH, adjacent columns are held together by weak CH···N hydrogen bonds (Fig. 2f, Table S9 SI). At variance with DNH, quinoline nitrogen atoms do not accept hydrogen bonded contacts, which rather involve just one pyridazine nitrogen (either N3 or N22, Figs. 1–2).

Packing energies

Quantitative energy analysis is necessary to understand what interactions prevail in determining the structure. In general, TNH has more negative lattice energy than DNH (Table 2). Both the force fields available in MiCMoS predict a difference of ~ 12–16 kJ·mol^{-1} (~ 2.9–3.8 kcal·mol^{-1}) per molecule in favor of TNH, regardless of whether the calculation is carried out on the static X-ray structures, or whether the estimate comes as an average over the last 200 ps of the MD simulations at 298 K.

The PIXEL energies, whose accuracy is more comparable with quantum mechanical models [53], are even closer, with difference not exceeding 4 kJ·mol^{-1} (~ 1 kcal·mol^{-1}) per molecule (Table 2). Dissection into individual energy contributions shows that more negative cohesive energies always come with a significant gain in electrostatic terms E_{el} (Coulomb + polarization), paralleled also by slightly more favorable Lennard–Jones interactions E_{LJ} (dispersion + repulsion). Both static CLP and PIXEL calculations ascribe this gain to electrostatics, as E_{el} terms are more negative in TNH by some kJ·mol^{-1} per molecule, while E_{LJ} remain almost equal within ~ 1 kJ·mol^{-1} per molecule (Table 2). The LJC force field agrees with the other methods in estimating a significantly more negative E_{el} in TNH (by up to 5–8 kJ·mol^{-1} per molecule) but predicts a considerable gain of dispersive energy as well (up to 8–9 kJ·mol^{-1} per molecule, Table 2). The reason for this apparent discrepancy resides in how the various energy terms are partitioned in the available functionals of the force field (see the first note to Table 2). At variance with both CLP and PIXEL, LJC does not explicitly account for polarization terms, which instead are implicitly included in the Lennard–Jones functional [37]. In other words, any energy gain due to atomic polarization effects, as implied for example by favorable π···π stacking interactions, is necessarily included in the E_{LJ} functional by the LJC force field. This picture is consistent with possibly stronger stacking interactions in TNH, as highlighted by the qualitative geometric analysis (see above).

The key role of electrostatics can be traced back to the distribution of electrostatic potential in the title compounds (Fig. 3a). Skeletal substitution of CH groups in 7,8 with nitrogens strongly polarizes the electron density distribution, accumulating negative charges in the region of the pyridazine ring (Fig. 3a, Table S10 SI). Accordingly, MP2/6-31G(p,d) calculations on the isolated molecules at their X-ray geometries predict that DHA is essentially apolar, with a dipole moment of ~ 0.5 D, while TNH exhibits a roughly tenfold increase of the dipole moment (~ 4.7 D, Figure S3 SI). The enhanced polarity of TNH was indeed

Table 2 Cohesive energies (E_{coh}) (kJ·mol^{-1} per molecule) of DNH and TNH, from both static and dynamic calculations, with dissection in terms of individual Coulomb (E_{C}), dispersive (E_{dis}), repulsive (E_{rep}) contributions

	Method[a]	E_{C}	E_{pol}	E_{el}[b]	E_{dis}	E_{rep}	E_{LJ}[c]	E_{coh}[d]
DNH	Static, LJC [37]	−14.3	-	−14.3	−193.8	77.0	−116.8	−131.0
	Static, CLP [34]	−15.6	−15.1	−30.7	−157.8	45.3	−112.5	−143.2
	Static, PIXEL [39]	−44.5	−20.0	−64.5	−176.5	99.7	−76.8	−141.2
	MD, LJC[e]	−13.2(1)	-	−13.2(1)			−107.7(2)	−120.9(2)
TNH	Static, LJC [37]	−18.9	-	−18.9	−205.2	80.5	−124.7	−143.6
	Static, CLP [34]	−21.2	−19.2	−40.4	−159.1	45.7	−113.4	−153.8
	Static, PIXEL [39]	−44.8	−22.4	−67.2	−169.1	91.0	−78.1	−145.2
	MD, LJC[e]	−20.7(1)	-	−20.7(2)			−116.4(3)	−137.1(3)

[a] Atom-atom energies, E_{ij}, read $E_{ij}(CLP) = \frac{q_i q_j}{R_{ij}} + \frac{A12}{R_{ij}^{12}} - \frac{A6}{R_{ij}^{6}} - \frac{A4}{R_{ij}^{4}}$ and $E_{ij}(LJC) = \frac{q_i q_j}{R_{ij}} + \frac{A12}{R_{ij}^{12}} - \frac{A6}{R_{ij}^{6}}$, being q_i, q_j point atomic charges, An empirical 4–6–12 coefficients and R_{ij} the atom–atom distances. PIXEL employs an expression analogue to CLP but exploits interactions among charge density "pixels", rather than individual atoms. Atomic polarization energy (the R^{-4} term) is not explicitly modelled in LJC. See MiCMoS users' manual [35] and Literature [37, 39] for more details

[b] Total electrostatic energy, $E_{\mathrm{el}} = E_{\mathrm{C}} + E_{\mathrm{pol}}$ (if applicable, see above)

[c] Total Lennard–Jones potential, $E_{\mathrm{LJ}} = E_{\mathrm{dis}} + E_{\mathrm{rep}}$

[d] Total cohesive energy, $E_{\mathrm{coh}} = E_{\mathrm{C}} + E_{\mathrm{pol}} + E_{\mathrm{dis}} + E_{\mathrm{rep}} = E_{\mathrm{el}} + E_{\mathrm{LJ}}$

[e] Average from last 200 ps of 500 ps-long *NpT* Molecular Dynamics trajectories at room temperature. Dispersion and repulsion energies are aggregated. Values in parentheses correspond to 1 estimated standard deviation

exploited already to drive specific interactions with a perhalogenated alkane [48].

Figure 3b shows the PIXEL in-crystal molecule–molecule interaction energies, E_{ij}, as a function of their center of mass (COM) distance. Each point on the graph matches a symmetry-related molecular pair, which can be either homochiral (full dots) or heterochiral (*i.e.* a pair of enantiomers, empty dots). Some points are worth noting. First, molecular pairs with COM distance up to 10 Å provide the most stabilizing contributions to the cohesive energy in both systems. These in fact correspond to the most relevant peaks at short distance of the COM radial distribution functions, g(r), as highlighted by MD simulations (Figs. 3c-d).

Second, all the close packed (and most stable) pairs, which correspond to the first two peaks of $g(r)$ in both graphs (D1-D2 and T1-T2), involve only enantiomers. All the homochiral pairs are never closer than ~9 Å (weak peaks D3 and T3), and provide allegedly less important stabilizing contributions, which do not exceed ~20 (TNH) or ~10 (DNH) kJ·mol^{-1} – the same order of magnitude of weak or moderate hydrogen bonds. [54] Third, and most important, TNH exploits more stable interactions between close enantiomer pairs, including its asymmetric unit (ASU) itself (Fig. 3b). This is due to favorable dipole–dipole interactions involving enantiomers in TNH (Figure S3 SI and Tables S11-S13 SI), while differences in the dispersive contributions are

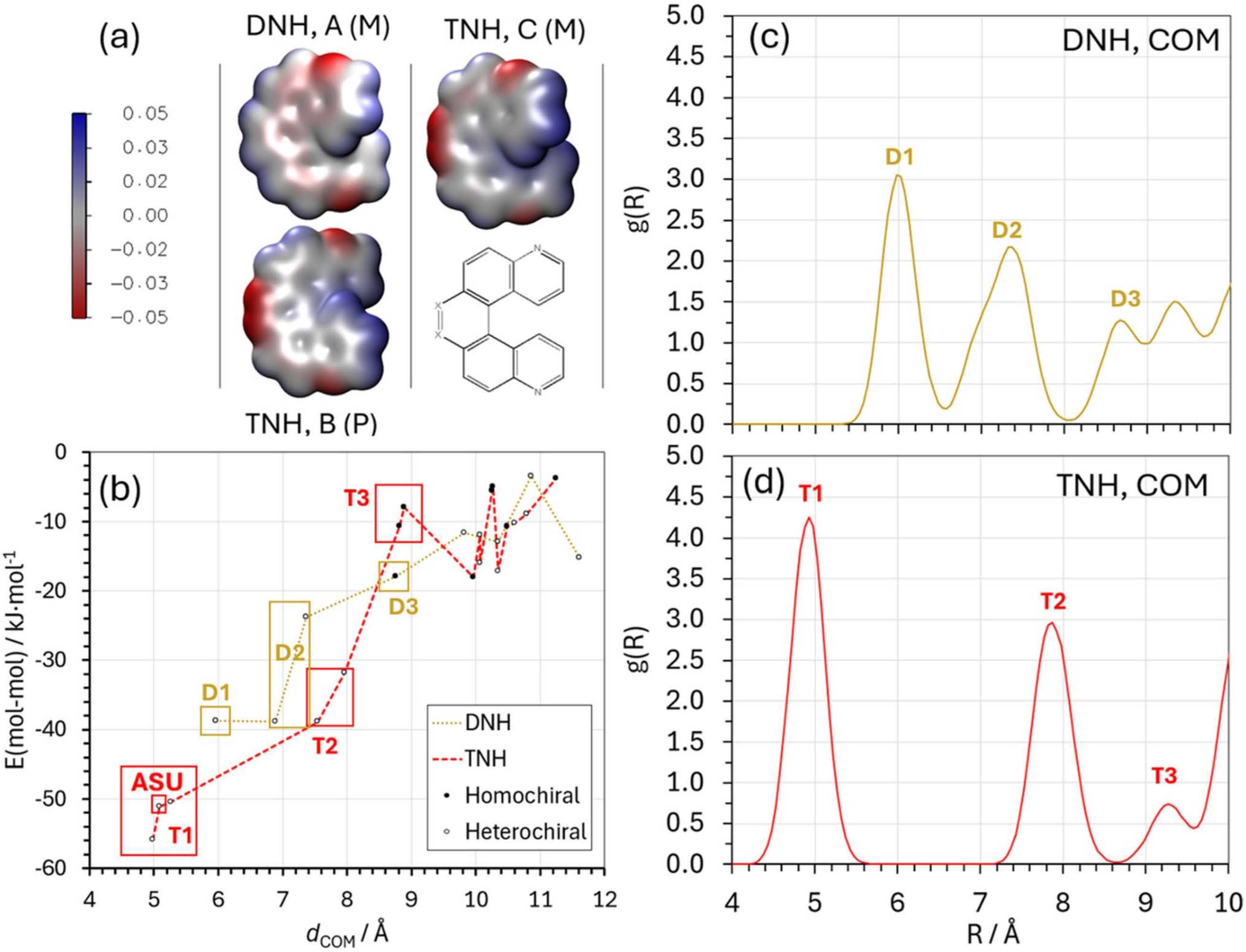

Fig. 3 Electrostatic potential mapped onto the 0.001 charge density isosurfaces of symmetry-independent molecules of DNH and TNH. Both scalar fields were evaluated at the MP2/6-31G(p,d) level of theory at the experimental X-ray geometries and expressed in atomic units (au), where 1 au = 6.7483 e·Å^{-3} for charge density and 1 au = 2625.5 kJ·mol^{-1} for electrostatic potential. Red (blue) colors highlight regions of negative (positive) electrostatic potential. In the molecular scheme, X = C-H for DNH and X = N for TNH. (b) Total molecule–molecule energies (kJ·mol^{-1}) from PIXEL calculations against the X-ray structures as a function of the molecular center of mass distance. Numerical entries are shown in Tables S11–S13 SI and in Figure S4 SI. Dashed lines serve only as guides for the eye. Homochiral (heterochiral) pairs are shown as full (empty) dots. Yellow (DNH) and red (TNH) boxes highlight molecular pairs that fall into specific peaks (see labels) of the corresponding radial distribution functions, as retrieved from MD simulations. (c-d) Radial distribution functions, $g(r)$, for molecular center of mass (COM), as a function of the center of mass distance. Labels D1-3 and T1-3 serve just to identify peaks and correspond to the boxes shown in Fig. 3b

generally smaller and not monotonic (compare for example purple and green lines in Figure S4 SI). Interestingly, the curves of electrostatic energies (Figure S4 SI, orange and blue lines) cross at ~ –6 kJ·mol^{-1} at around 9 Å, meaning that the closest homochiral pairs are equally (and weakly) stabilized by electrostatics in both crystals.

A take-home message from these results is that the significantly greater polarity of TNH dictates its crystal packing. Antiparallel arrangements of polar molecules are favored by second-kind symmetry elements [55], which establish strongly bonded enantiomeric pairs. The electrostatic-driven closer proximity of adjacent molecules in TNH facilitates the setup of stacking interactions between facing aromatic rings. On the contrary, the very low polarity of DNH makes dispersive contributions prevail, and in fact these are almost invariably more negative than the electrostatic ones (Figure S4 SI). The packing of DNH results from the best tradeoff between shape effects, which call for glide operators to fit left-handed with right-handed structures, and attractive van der Waals contributions, possibly enhanced by (weaker) stacking interactions. Finally, weak CH···N hydrogen bonds connect glide-related molecules in both crystals (Tables S9 SI and S11-S13 SI) but their contribution is barely significant. In fact, hydrogen-bonded pairs are systematically overwhelmed by closer pairs without hydrogen bonds, which provide significantly more negative molecular contributions to cohesive energy. This evidence raises a warning against relying on pure geometrical criteria, including analysis of HSFP, to determine what interactions are significant to explain cohesion in crystals. [56]

Chiral forms of the title compounds: A CSP study

It is often reported that racemic crystallization is largely preferred over formation of enantiomerically pure conglomerates [57, 58]. Azahelicenes are usually consistent with this general trend [59, 60]. In fact, to the best of our knowledge, homochiral crystals of DNH and TNH were never characterized to date. However, it is known that racemic crystals are not necessarily more stable than their homochiral counterpart. [61] Understanding how energetic and packing factors [62–64] contribute to homochiral crystallization is mandatory to design the best synthetic strategy toward the desired optically active materials. [65] In this context, we generate enantiopure models for the title compounds, with the purpose of providing a tentative – and motivated – answer to the question of whether the crystallization of homochiral DNH and TNH is even experimentally plausible or not. We restricted our screening to $P2_1$ and $P2_12_12_1$ space groups, which host most frequently enantiomerically pure substances, [66] and to Z'=1 structures, to deal with predictions comparable on the same grounds. Tables S15 and S16 SI list the 20 top-ranking structures for each prediction.

Figure 4a shows the structural landscape obtained through the SC-MC method [46]. A general linear correlation is appreciable between cohesive energy and packing efficiency, as expected. $P2_12_12_1$ structures (squares in Fig. 4a) tend to achieve greater absolute cohesive energies and C_{pack} than $P2_1$ ones, likely mirroring the greater availability of accessible packing modes in the higher-order symmetry. However, as usual, [61] this is just a general trend more than a rule. In analogy with experimental findings, TNH crystals (blue dots) often display greater cohesion than DNH (red dots), most likely due to more favorable electrostatics (see above). In any case, the title compounds follow Wallach rule, [67] meaning that experimental racemic crystals are more closely packed (and have higher density and greater, or comparable, $|E_{\mathrm{coh}}|$) than homochiral ones. In most $P2_1$ top-ranking predictions, both substances form parallel stacks of aromatic rings piled up along either *a* or *c* axes, allegedly exploiting favorable aromatic π···π interactions. In $P2_12_12_1$ the packing is more complex, but there is always is at least one crystallographic direction where patent stacking interactions are set up. Figure S8 SI provides some examples.

An important point is that the space group $P2_1$ is polar and admits nonzero dipole moment in the unit cell, in principle paving the way to the design of TNH-based pyroelectric or ferroelectric materials. Unfortunately, this seems not so likely. Most top-ranking SC-MC predictions for TNH in $P2_1$ consistently bear immaterial (<<1 D) cell dipole moments, since individual molecular dipoles (Figure S9 SI) preferentially lie orthogonal to the unique screw operator along the monoclinic cell axis. Interestingly, this ensures an energetically stable antiparallel arrangement of dipoles (see for example Figure S9a SI), analogue to that imposed by second-kind symmetry operators in the experimental *Pbca* and $P2_1/c$ lattices. Though, there are some exceptions. For example, the 5th-rank $P2_1$ structure (Figure S9b SI) has nonzero cell dipole (~7 D), which contributes by ~4 kJ·mol^{-1} per molecule to the total cohesive energy.

In general, results from brute-force approaches, including those shown in Fig. 4a, should be considered with caution. To get rid of possible inadequacies of the SC-MC algorithm, particularly of those due to the imposed rigidity of the molecular building blocks, the inclusion of thermal effects is mandatory. [46] Actually, we expect that stable structures lie on reasonably deep potential energy wells. MD allows to check the mechanical stability of the predicted structures by probing the curvature of the potential around the Monte Carlo minimum, with the pros and cons of the same classical force field. Thus, each prediction within the first 10 top-ranked structures underwent 200 ps of MD relaxation (see Methods). Relevant results, together with the new ranking, are shown in Fig. 4b. The first indication of the role of

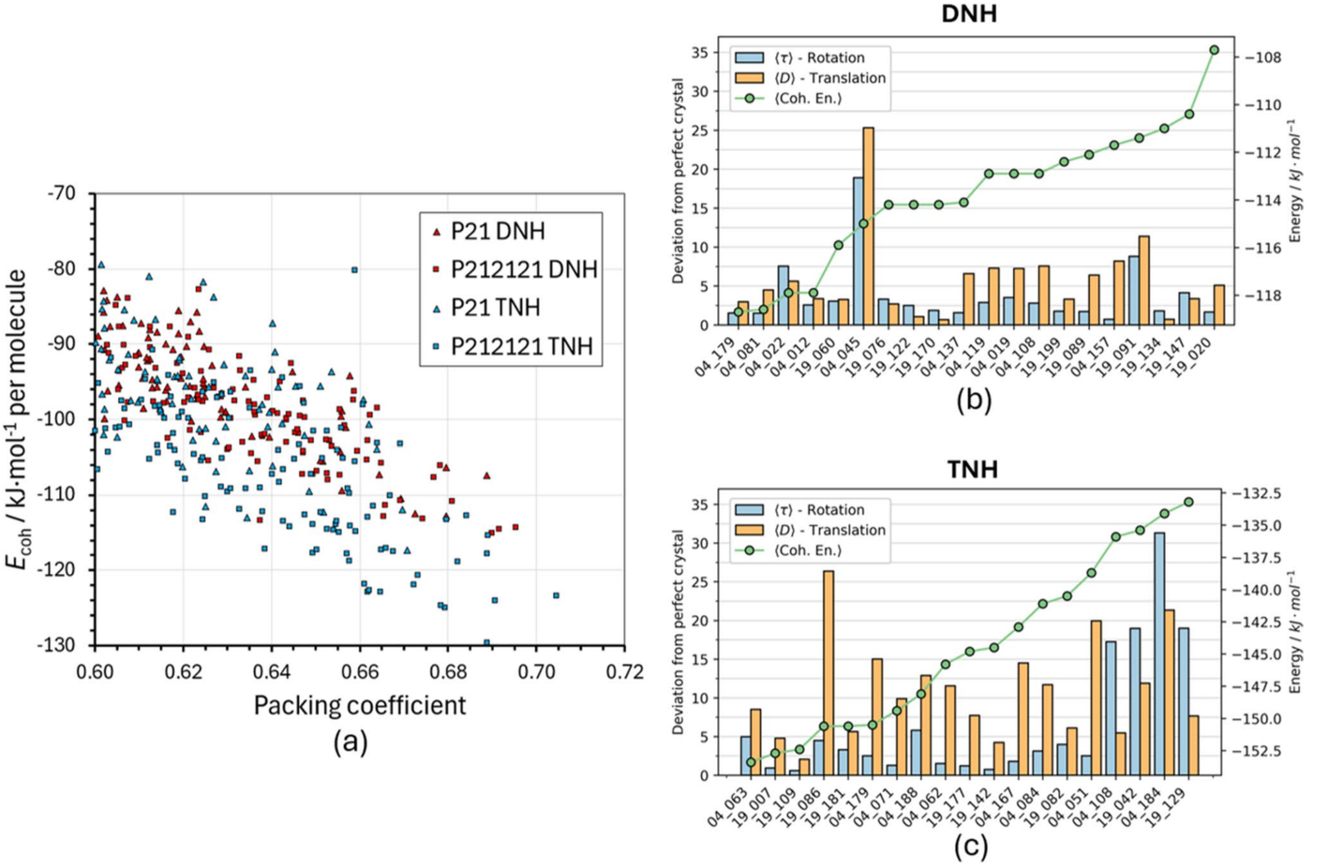

Fig. 4 Structural landscape for possible homochiral structure of DNH and TNH, as estimated by the Symmetry-Constrained Monte Carlo (SC-MC) algorithm. [46] (a) Cohesive energies (kJ·mol^{-1} per molecule) *vs*. packing coefficient (C_{pack}) for all the unique SC-MC predictions with $C_{pack} \geq 0.6$ (duplicates removed). Red (blue) dots refer to DNH (TNH), while triangles (squares) represent the $P2_1$ ($P2_12_12_1$) space group. All predictions are based on static X-ray geometries, *i.e.* no relaxation of the molecular conformation was allowed. To the sake of comparison, $C_{pack} = 0.73$ for experimental DNH in *Pbca* and 0.74 for experimental TNH in $P2_1/c$. (b-c) Final energy ranking for the most promising DNH (panel b) and TNH (panel c) structures after applying Molecular Dynamics to top-ranked predictions in (a). Structures are labelled as XX_YYY, where XX is the space group number, and YYY is the cardinal number of the generated structure. The different structures are ranked in terms of energy from left to right. The primary y-axis indicates the difference in terms of rotational (‹τ›, %) and translational (‹D›, Å) coefficients from the perfect crystal; the secondary y-axis reports the average cohesive energy (‹E_{coh}›). The molecular vectors used to calculate ‹τ› are reported in Figure S7 SI

dynamic effects emerges from the structure relaxation, evident in the absolute energy scale. For DNH, the minimum remains essentially unchanged (–119 kJ mol^{-1}, in line with SC–MC values of ~ –115 kJ mol^{-1}). In contrast, TNH undergoes a marked stabilization, with the most stable structure shifting from –130 to –152.5 kJ mol^{-1} per molecule, corresponding to a gain of more than 20 kJ mol^{-1} per molecule.

For DNH, two pairs of energetically equivalent structures were identified, all belonging to the $P2_1$ space group. The 1 st, 2nd, and 4th–ranked structures showed reasonable mechanical stability, with rotational correlations below ~ 2.5% and translational deviations under 5 Å, consistent with good crystallinity. The 3rd–ranked structure displayed larger displacements (7.5% rotational and 5.0 Å translational) and was discarded. The packing modes of these 4 structures are similar: the helicenes pack along the *a*-axis, with the formation of π- π interactions of translation-related molecules with different tilting angles. Weak but ubiquitarian C-H···N and C-H···π interactions are set up along the other directions, connecting different pillars. The packing motifs are reported in Figures S10 and S11, Supporting Information. As expected, the top-ranking $P2_1$ structures after thermalization are all essentially apolar (Table S17 SI), with cell dipole moments never exceeding 1 D. The cohesive energy of the highest-ranked structure after MD relaxation is approximately − 119 kJ·mol^{-1}, which is comparable to that of the racemate (≈ − 121 kJ·mol^{-1}; Table 2). The similarity in energy arises from the low polarity of DNH molecules, with dispersion interactions providing the dominant contribution to the total cohesive energy. The small energy difference, which lies within the intrinsic accuracy of the chosen force field (≈ 5 kJ·mol^{-1}) [34], does not allow any definitive conclusion to be drawn regarding the relative energetic stability of the enantiomerically pure and racemic structures.

Similar conclusions can be drawn for TNH. Figure 4b shows 3 nearly isoenergetic structures, with an energy gap of ~ 1 kJ mol^{-1} with the 4th one. The lowest-energy structure exhibits poor crystallinity, with rotational and translational discrepancies of ~ 5% and 10 Å, respectively. Between the second and third ranked structures, the latter proves mechanically more stable. Both belong to the $P2_12_12_1$ space group, which enforces a null dipole moment, aside from minor numerical deviations introduced by molecular dynamics. The polar (μ_{cell} ~ 7 D) structure mentioned above and ranking as 5th in the static SC-MC prediction, shifts to the 18th position once dynamic effects are considered, and shows strong mechanical instabilities (Fig. 4c, structure 04_184). This outcome highlights once more the importance of including molecular dynamics in CSP workflows, as dynamic effects are essential for a reliable assessment of both the energetic ranking and the mechanical stability of the predicted crystal forms. From a structural viewpoint, the top-ranked $P2_1$ form has a similar packing detected for the DNH compound and exploits a cell dipole moment of ~ 1.6 D, while in the next four $P2_12_12_1$ structures π-stacking motifs are built between C_2-related molecules (see Figures S10 and S11 SI). As for TNH, the cohesive energy of the highest-ranked structure after MD relaxation (− 153.4 kJ·mol^{-1}) differs significantly from that of the racemic crystal (− 137.1 kJ·mol^{-1}, Table 2). Thus, the enantiomerically pure polymorph is predicted to be thermodynamically more stable than the corresponding racemate. A decomposition of the cohesive energy reveals that this stabilization is mainly driven by the Lennard–Jones contribution, which amounts to − 151.5 kJ·mol^{-1}, substantially larger than the corresponding value observed for the racemic form (E_{LJ} = − 116.3 kJ·mol^{-1}, Table 2). In contrast, the Coulombic contribution in the enantiopure crystal is nearly negligible (− 1.9 kJ·mol^{-1}), whereas a significantly larger electrostatic contribution is found in the racemate (− 20.7 kJ mol^{-1}). These results indicate that the enantiomerically pure crystal adopts a more efficient packing motif, which does not maximize electrostatic interactions associated with the relatively large molecular dipole moment of TNH, but instead favors dispersion-dominated stabilization. As a result, enhanced packing efficiency leads to a lower overall cohesive energy. The case of TNH provides a further example of how the crystal packing of an organic substance depends, often in a non-trivial way, on a subtle interplay of competitive intermolecular interactions [68]. However, it must be stressed that, despite this predicted thermodynamic preference, the enantiomerically pure form of TNH has not been experimentally observed to date.

In conclusion, $P2_1$ structures seem to be favored for both compounds, even though some $P2_12_12_1$ lattices cannot be excluded for TNH. In any case, no unquestionable evidence of pyroelectric behavior was found in energetically and mechanically stable crystal forms of enantiomerically pure TNH and DNH. Such predictions wait for experimental confirmation and possibly call for a full study of the crystal structure landscape to be confirmed.

Conclusions

In this work, a thorough crystal chemical study was carried out on two symmetrically nitrogenated [5]helicenes, namely 4,11-diaza[5]helicene (DNH) and 4,7,8,11-tetraaza[5]helicene (TNH). Their crystal structure was accurately determined by X-ray diffraction at room temperature. Experiments were complemented by both quantum mechanical calculations at the MP2/6-31G(p,d) level and classical force-field based simulations, to retrieve as much accurate intermolecular interaction energies.

It was found that the conformation of the [5]helicene scaffold does not depend on nitrogen substitution in positions 7 and 8. Therefore, differences in the crystal packing can be genuinely attributed to the skeletal replacement of two CH groups in 7,8. with nitrogen atoms. Both crystals are centrosymmetric racemates and contain an equimolar amount of P and M enantiomers, as expected owing to the non-enantioselective synthesis procedure. Both crystals exploit stacked columnar arrangements of aromatic rings to achieve efficient packing and differ in how such stacking motifs are mutually oriented, as well as in the relative distance between facing rings. TNH exhibits closer packing and greater cohesion. Weak CH···N hydrogen bonds are also present, but they are overwhelmed by stronger contributions to cohesive energies and barely bear any structural significance.

In TNH, electrons are accumulated in the central pyridazine ring, polarizing the static density so that a tenfold increase in the molecular dipole moment is observed. Accordingly, the TNH crystal is dominated by antiparallel packing of adjacent dipole moments. The attractive dipole–dipole interactions present in TNH, which are entirely absent in DNH, likely draw neighboring molecules closer together. This leads to a significant ~ 5% increase in crystal density compared to DNH.

Finally, the crystal structure landscape of both compounds was explored by the recently developed SC-MC algorithm, to look for plausible homochiral forms in common $P2_1$ and $P2_12_12_1$ space groups. Based on energy ranking and Molecular Dynamics simulations, enantiomerically pure DNH and TNH might indeed crystallize in some $P2_1$ forms, although patent polar forms are improbable. TNH can in principle also have $P2_12_12_1$ forms that are favored both thermodynamically and mechanically. We are aware that the present screening is necessarily partial, as real-life scenarios might require to consider other Sohncke groups. For sure, our predictions suggest that homochiral forms of the title compounds will likely imply significant stacking motifs, while TNH should exploit first-kind symmetry elements to maximize the antiparallel pairing of molecular dipole moments. This information could be of some use in future crystallization screening experiments, for example to select solvents or solvent mixtures with the proper polarity.

The problem of why Z'=2 in TNH and Z'=1 in DNH remains open. As suggested by one Reviewer, $P2_1/c$ (TNH) is a maximal non-isomorphic subgroup of *Pbca* (DNH). This implies that more efficient packing is related to the loss of a coset of symmetry elements, which allows to lose the symmetry of first-neighbor molecular pairs. Extensive experimental screening of the crystal structure landscape would be useful to gain further insights on this matter.

Supplementary Information The online version contains supplementary material available at https://doi.org/10.1007/s11224-026-02724-6.

Acknowledgements L.L.P. and G.M. wish to thank prof. Angelo Gavezzotti for continuous inspiration and encouragement. Università degli Studi di Milano is also acknowledged for funding this research through the program “Piano di sostegno alla ricerca 2023-2024” (grant number PSR2023_DIP_005_PI_LLOPR). The Unitech@unimi technological platform COSPECT is warmly acknowledged for provision of X-ray beamtime.

Author contributions F. F., M.P. and S.R.: Conceptualization, Resources, Investigation, Project Administration. L.S., M.V.: Formal analysis, Investigation, Writing – Review & Editing. G.M.: Formal analysis, Investigation, Supervision, Writing – Review & Editing. L.L.P.: Conceptualization, Funding acquisition, Project administration, Supervision, Writing – Original Draft.

Funding Open access funding provided by Università degli Studi di Milano within the CRUI-CARE Agreement. Funding for open access was kindly provided by Università degli Studi di Milano through the CRUI-CARE Agreement. The Chemistry Department is acknowledged for funding this work through the Atheneum Research Support Plan (Piano di Sostegno alla Ricerca) 2023, grant number PSR2023_DIP_005_PI_LLOPR.

Data availability Relevant steering parameters and procedures for computer simulations described in this paper are deposited in the Supporting Information. Molecular dynamics trajectories and outputs of quantum chemical simulations can be downloaded freely from the public repository Zenodo (https://doi.org/10.5281/zenodo.17407385).

Declarations

Ethics approval Not applicable, as no human participants or animals were involved in this research.

Competing interests The authors declare no competing interests.

References

1. 'Helicity' in *IUPAC Compendium of Chemical Terminology*, 5th ed. International Union of Pure and Applied Chemistry; Online version 5.0.0, 2025. Last accessed: 25/08/2025. https://doi.org/10.1351/goldbook.H02763
2. Watanabe H, Sakami T, Iwakura A, Nakashima Y, Nishinaka M, Morimoto H, Nakashima S, Okuda Y, Iwanaga T, Akashi H, Orita A (2025) Modular synthesis of substituted [n]helicenes (n = 5–7) starting from arylmethyl sulfone and arylene dialdehyde: aldol-type condensation, photocyclization, and desulfonylative arylation. J Org Chem 90:9002–9013
3. Sahasithiwat S, Mophuang T, Menbangpung T, Kamtonwong S, Sooksimuang T (2010) 3,12-Dimethoxy-7,8-dicyano-[5]helicene as a novel emissive material for organic light-emitting diode. Synth Met 160:1148–1152
4. Petdum A, Panchan W, Swanglap P, Sirirak J, Sooksimuang T, Wanichacheva N (2018) “Turn-ON” [5]helicene-based fluorescence sensor with very large Stokes shift for highly selective detection of Ag+ and AgNPs. Sens Actuators, B Chem 259:862–870
5. Lewińska G, Danel KS, Sanetra J (2016) The bulk heterojunction cells based on new helicenes – preparation, implementation and surface examination. Sol Energy 135:848–853
6. Isla H, Saleh N, Ou-Yang J-K, Dhbaibi K, Jean M, Dziurka M, Favereau L, Vanthuyne N, Toupet L, Jamoussi B, Srebro-Hooper M, Crassous J (2019) Bis-4-aza[6]helicene: a bis-helicenic 2,2′-bipyridine with chemically triggered chiroptical switching activity. J Org Chem 84:5383–5393
7. Peng Z, Takenaka N (2013) Applications of helical-chiral pyridines as organocatalysts in asymmetric synthesis. Chem Record 13:28–42
8. Zhang G, Zhang J, Tao Y, Fuwei G, Geyu L, Juncong L, Chengshuo C, Yuebiao Z, Huibin Q (2024) Facile fabrication of recyclable robust noncovalent porous crystals from low-symmetry helicene derivative. Nat Commun 15:5469
9. Storch J, Zadny J, Strasak T, Kubala M, Sykora J, Dusek M, Cirkva V, Matejka P, Krbal M, Vacek J (2014) Synthesis and characterization of a helicene-based imidazolium salt and its application in organic molecular electronics. Chem Eur J 21:2343–2347
10. Tanaka K, Osuga H, Kitahara Y (2000) Clathrate formation by and self-assembled supramolecular structures of a “molecular spring”. J. Chem. Soc. Perkin Trans 2:2492–2497
11. Yan Q, Tao S, Liu R, Zhi Y, Jiang D (2023) Crystalline, porous helicene covalent organic frameworks. Angew Chem Int Ed 63:e202316092
12. Qiu M, Du J, Yao N-T, Wang X-Y, Gong H-Y (2025) Advances in nitrogen-containing helicenes: synthesis, chiroptical properties, and optoelectronic applications. Beilstein J Org Chem 21:1422–1453

13. Balakhonov RY, Gaeva EB, Mekeda IS, Dolotov RA, Metelitsa AV, Shirinian VZ (2024) Structure and photophysical properties of furoquinoline aza-helicenes: fluorescence enhancement by protonation. Dyes Pigments 225:112032
14. Taniguchi T, Nishii Y, Mori T, Nakayama K-i, Miura M (2021) Synthesis, structure, and chiroptical properties of indolo- and pyridopyrrolo-carbazole-based C2-symmetric azahelicenes. Chem Eur J 27:7356–7361
15. Maeda C, Ema T (2025) Recent development of azahelicenes showing circularly polarized luminescence. Chem Commun 61:4757–4773
16. Abbate S, Longhi G, Lebon F, Castiglioni E, Superchi S, Pisani L, Fontana F, Torricelli F, Caronna T, Villani C, Sabia R, Tommasini M, Lucotti A, Mendola D, Mele A, Lightner DA (2014) Helical sense-responsive and substituent-sensitive features in vibrational and electronic circular dichroism, in circularly polarized luminescence, and in Raman spectra of some simple optically active hexahelicenes. J Phys Chem C 118:1682–1695
17. Irfan A, Assiri M, Al-Sehemi AG (2018) Exploring the optoelectronic and charge transfer performance of diaza[5] helicenes at molecular and bulk level. Org Electron 57:211–220
18. Tanaka K, Osuga H, Kitahara Y (2000) Clathrate formation by and self-assembled supramolecular structures of a “molecular spring.” J Chem Soc, Perkin Trans 2:2492–2497
19. Karak P, Choudhuri J (2022) Conformationally flexible heterohelicenes as stimuli-controlled soft molecular springs. Chem Sci 13:1163–1173
20. Bazzini C, Brovelli S, Caronna T, Gambarotti C, Giannone M, Macchi P, Meinardi F, Mele A, Panzeri W, Recupero F, Sironi A, Tubino R (2005) Synthesis and characterization of some aza[5] helicenes. Eur. J. Org. Chem. 7:1247–1257
21. Bazzini C, Caronna T, Fontana F, Macchi P, Mele A, Natali Sora I, Panzeri W, Sironi A (2008) Synthesis, crystal structure and crystal packing of diaza[5]helicenes. New J Chem 32:1710–1717
22. Caronna T, Castiglione F, Fontana F, Famulari A, Malpezzi L, Mele A, Mendola D, Natali Sora I (2012) Quantum mechanics calculations, basicity and crystal structure: the route to transition metal complexes of azahelicenes. Molecules 17:463–479
23. Kitaigorodskii AI (1965) The principle of close packing and the condition of thermodynamic stability of organic crystals. Acta Crystallogr 18:585–590
24. Galbraith HV, Degering EF, Hitch EF (1951) The alkaline reduction of aromatic nitro compounds with glucose. J Am Chem Soc 73:1323–1324
25. Farrar W V (1965) Polycyclic Reduction Products of 6-Nitroquinoline. J. Chem. Soc., 799–800
26. Rummens FHA, Bellaart AC (1967) The structure of “azodichinyl.” Tetrahedron 23:2735–2738
27. Bellaart AC (1964) Reduction of 6-nitroquinoline with phosphine. Rec Trav Chim Pays-Bas 83:718–722
28. Sheldrick GM (2015) Crystal structure refinement with SHELXL. Acta Crystallogr Sect C Struct Chem 71:3–8
29. Spek AL (2003) Single-crystal structure validation with the program PLATON. J Appl Crystallogr 36:7–13
30. Spackman PR, Turner MJ, McKinnon JJ, Wolff SK, Grimwood DJ, Jayatilaka D, Spackman MA (2021) *Crystalexplorer*: a program for Hirshfeld surface analysis, visualization and quantitative analysis of molecular crystals. J Appl Cryst 54:1006–1011
31. Bruno IJ, Cole JC, Edgington PR, Kessler M, Macrae CF, McCabe P, Pearson J, Taylor R (2002) New software for searching the Cambridge Structural Database and visualizing crystal structures. Acta Crystallogr Sect B Struct Sci Cryst Eng Mater 58:389–397
32. Macrae CF, Sovago I, Cottrell SJ, Galek PTA, McCabe P, Pidcock E, Platings M, Shields GP, Stevens JS, Towler M, Wood PA (2020) Mercury 4.0: from visualization to analysis, design and prediction. J Appl Crystallogr 53:226–235
33. Gavezzotti A, Lo Presti L, Rizzato S (2022) Molecular dynamics simulation of organic materials: structure, potentials and the MiCMoS computer platform. CrystEngComm 24:922–930
34. Gavezzotti A, Lo Presti L (2019) Molecular dynamics simulation of organic crystals: introducing the CLP-dyncry environment. J Appl Cryst 52:1253–1263
35. Lo Presti L, Macetti G, Sironi L, Vacchini M (2025) MiCMoS v2.4 Users’ Manual, https://sites.unimi.it/xtal_chem_group/index.php/research/5-micmos. Accessed on August 14, 2025
36. Allen FH, Bruno IJ (2010) Bond lengths in organic and metal-organic compounds revisited: X-H bond lengths from neutron diffraction data. Acta Crystallogr Sect B Struct Sci 66:380–386
37. Gavezzotti A, Lo Presti L, Rizzato S (2020) Mining the Cambridge database for theoretical chemistry. Mi-ljc: a new set of Lennard-jones–coulomb atom–atom potentials for the computer simulation of organic condensed matter. CrystEngComm 22:7350–7360
38. Gavezzotti A (2008) Bond lengths in organic and metal-organic compounds revisited: X-H bond lengths from neutron diffraction data. Mol Phys 106:1473–1485
39. Gavezzotti A (2005) Calculation of lattice energies of organic crystals: the PIXEL integration method in comparison with more traditional methods. Zeitschrift für Kristallographie - Crystalline Materials 220:499–510
40. Brennan CM, Wilberg KB (1990) Determining atom-centered monopoles from molecular electrostatic potentials. The need for high sampling density in formamide conformational analysis. J Comput Chem 11:361–373
41. Frisch M J, Trucks G W, Schlegel H B, Scuseria G E, Robb M A, Cheeseman J R, Scalmani G , Barone V , Petersson G A , Nakatsuji H, Li X, Caricato M, Marenich A V, Bloino J, Janesko B G, Gomperts R, Mennucci B, Hratchian H P, Ortiz J V, Izmaylov A F, Sonnenberg, J L, Williams-Young D, Ding F, Lipparini F, Egidi F, Goings J, Peng B, Petrone A, Henderson T, Ranasinghe D, Zakrzewski V G, Gao J, Rega N, Zheng G, Liang W, Hada M, Ehara M, Toyota K, Fukuda R, Hasegawa J, Ishida M, Nakajima T, Honda Y, Kitao O, Nakai H, Vreven T, Throssell K, Montgomery J A Jr, Peralta J E, Ogliaro F, Bearpark M J, Heyd, J J, Brothers E N, Kudin K N, Staroverov V N, Keith T A, Kobayashi R, Normand J, Raghavachari K, Rendell A P, Burant J C, Iyengar S S, Tomasi J, Cossi M, Millam J M, Klene M, Adamo C, Cammi R, Ochterski J W, Martin, R L, Morokuma K, Farkas O, Foresman J B, Fox D J (2016) Gaussian 16, Revision C.01, Gaussian, Inc., Wallingford CT
42. Humphrey W, Dalke A, Schulten K (1996) VMD - Visual Molecular Dynamics. J Mol Graph 14:33–38
43. Bussi G, Donadio D, Parrinello M (2007) Canonical sampling through velocity rescaling. J Chem Phys 126:014101
44. Parrinello M, Rahman A (1980) Crystal structure and pair potentials: a molecular-dynamics study. Phys Rev Lett 45:1196–1199
45. Gavezzotti A, Lo Presti L (2018) Dynamic simulation of liquid molecular nanoclusters: structure, stability and quantification of internal (pseudo)symmetries. New J Chem 43:2077–2084
46. Macetti G, Sironi L, Vacchini M, Lo Presti L (2025) Symmetry-Constrained Monte Carlo for the crystal structure prediction of small organic molecules. Cryst Growth Des 2025(25):8382–8392
47. Macetti G, Lo Presti L (2025) Symmetry constrained Monte Carlo Users’ Manual, v1 0, Università degli Studi di Milano Last accessed at 17/08/2025 on https://sites.unimi.it/xtal_chem_group/images/SC-MC/scmc_v1 0_manual pdf
48. Biella S, Cametti M, Caronna T, Cavallo G, Forni A, Metrangolo P, Pilati T, Resnati G, Terraneo G (2011) Site-selective assembly between 1,8-diiodoperfluorooctane and 4,7,8,11-tetraazahelicene driven by halogen bonding. Supramol Chem 23:256–262

49. Groom CR, Bruno IJ, Lightfoot MP, Ward SC (2016) The Cambridge Structural Database. Acta Crystallogr Sect B Struct Sci Cryst Eng Mater 72:171–179
50. Lo Presti L, Sist M, Loconte L, Pinto A, Tamborini L, Gatti C (2014) Rationalizing the lacking of inversion symmetry in a noncentrosymmetric polar racemate: an experimental and theoretical study. Cryst Growth Des 14:5822–5833
51. Barroso J, Cabellos JL, Pan S, Murillo F, Zarate X, Fernandez-Herrera MA, Merino G (2018) Revisiting the racemization mechanism in helicenes. Chem Commun 54:188–191
52. Spackman MA, Jayatilaka D (2009) Hirshfeld surface analysis. CrystEngComm 11:19–32
53. Dunitz J, Gavezzotti A (2009) How molecules stick together in organic crystals: weak intermolecular interactions. Chem Soc Rev 38:2622–2633
54. Lo Presti L On the significance of weak hydrogen bonds in crystal packing: a large databank comparison of polymorphic structures (2018) CrystEngComm 20: 5976–5989
55. Symmetry operation, in IUCr Online Dictionary of Crystallography (2025) The Commission for Crystallographic Nomenclature (CCN) of the International Union of Crystallography (IUCr). Accessed 18 Dec 2025. https://dictionary.iucr.org/Symmetry_operation
56. Macetti G, Sironi L, Lo Presti L (2024) Classical Molecular Dynamics Simulation of Molecular Crystals and Materials: Old Lessons and New Perspectives In: Yanez, Manuel and Boyd, Russell J (eds) Comprehensive Computational Chemistry, vol 3, pp 777–803 Oxford, Elsevier
57. Pérez-García L, Amabilino DB (2002) Spontaneous resolution under supramolecular control. Chem Soc Rev 31:342–356
58. Gavezzotti A, Lo Presti L (2015) Theoretical study of chiral carboxylic acids structural and energetic aspects of crystalline and liquid states. Cryst Growth Des 15:3792–3803
59. Rekis T (2020) Crystallization of chiral molecular compounds: what can be learned from the Cambridge Structural Database? Acta Crystallogr Section B: Structural Sci, Crystal Eng Mater 76:307–315
60. Yang Y, Rice B, Shi X, Brandt JR (2017) Correa da Costa R, Hedley G J, Smilgies D-M, Frost J M, Samuel I D W, Otero-de-la-Roza A, Johnson E R, Jelfs K E, Nelson J, Campbell A J, Fuchter M. J ACS Nano 11:8329–8338
61. Gavezzotti A, Rizzato S (2014) Are racemic crystals favored over homochiral crystals by higher stability or by kinetics? Insights from comparative studies of crystalline stereoisomers. J Org Chem 79:4809–4816
62. Macetti G, Loconte L, Rizzato S, Gatti C, Lo Presti L (2016) Intermolecular recognition of the antimalarial drug chloroquine: a quantum theory of atoms in molecules−density functional theory investigation of the hydrated dihydrogen phosphate salt from the 103 K X-ray structure. Cryst Growth Des 16:6043–6054
63. Gatti C, Macetti G, Boyd RJ, Matta CF (2018) An electron density source-function study of DNA base pairs in their neutral and ionized ground states. J Comput Chem 39:1112–1128
64. Wieduwilt EK, Boto RA, Macetti G, Laplaza R, Contreras-García J, Genoni A (2023) Extracting quantitative information at quantum mechanical level from noncovalent interaction index analyses. J Chem Theory Comput 19:1063–1079
65. Lorenz H, Seidel-Morgenstern A (2014) Processes to separate enantiomers. Angew Chem Int Ed Engl 53:1218–1250
66. Gavezzotti A (2007) Molecular aggregation structure analysis and molecular simulation of crystals and liquids. IUCr Monographs on Crystallography n 19 Oxford University Press. Great Clarendon Street, Oxford
67. Pratt Brock C, Schweizer WB, Dunitz JD (1991) On the validity of Wallach's rule: on the density and stability of racemic crystals compared with their chiral counterparts. J Am Chem Soc 113:9811–9820
68. Destro R, Sartirana E, Loconte L, Soave R, Colombo P, Destro C, Lo Presti L (2013) Competing C═O⋯C═O, C-H⋯O, Cl⋯O, and Cl⋯Cl interactions governing the structural phase transition of 2,6-dichloro-*p*-benzoquinone at Tc = 122 6 K. Cryst Growth Des 13:4571–4582